Simulated Particle Evolution within a Winter Storm: Contributions of Riming to Radar Moments and Precipitation Fallout

Andrew DeLaFrance[1], Lynn A. McMurdie[1], Angela K. Rowe[2], Andrew J. Heymsfield[3,4]

[1]Department of Atmospheric Sciences, University of Washington,

Seattle, WA, USA

[2]Department of Atmospheric and Oceanic Sciences, University of Wisconsin-Madison,

Madison, WI, USA

[3]National Center for Atmospheric Research,

Boulder, Co, USA

[4]U.S. National Science Foundation,

Alexandria, VA, USA

Correspondence to: Andrew DeLaFrance (adelaf@uw.edu)

Manuscript submitted 17 May 2024

Revised manuscript submitted 17 July 2024

Abstract

Remote sensing radars from air- and spaceborne platforms provide critical observations of clouds to estimate precipitation rates across the globe. Capability of these radars to detect changes in precipitation properties is advanced by Doppler measurements of particle fall speed. Within mixed-phase clouds, precipitation mass and its fall characteristics are especially sensitive to the effects of riming. In this study, we quantified these effects and investigated the distinction of riming from aggregation in Doppler radar vertical profiles using quasi-idealized particle-based model simulations. Observational constraints of a control simulation were determined from airborne in situ and remote sensing measurements collected during the Investigation of Microphysics and Precipitation for Atlantic Coast-Threatening Snowstorms (IMPACTS) for a wintry-mixed precipitation event over the northeast United States on 04 February 2022. From the upper boundary of a one-dimensional column, particle evolution was simulated through vapor deposition, aggregation, and riming processes, producing realistic Doppler radar profiles. Despite a modest observed amount of supercooled liquid water (0.05 g m^{-3}), riming accounted for 55% of the ice-phase precipitation mass, cumulatively increasing reflectivity by 44% and Doppler velocity by 68%. Independent evaluation of process-based sensitivities showed that while radar reflectivity is comparably sensitive to either riming- or aggregation-based particle morphology, the Doppler velocity profile is uniquely sensitive to particle density changes during riming. Thus, Doppler velocity profiles advance the diagnosis of riming as a dominant microphysical process in stratiform clouds from single-wavelength radars, which has implications for quantitative constraints of particle properties in remote sensing applications.

1. Introduction

Ice crystals within precipitating winter storms evolve through an inherently stochastic sequence of microphysical processes which uniquely affect their physical properties and fall characteristics. This continuous and process-based evolution of ice-phase particles remains poorly represented by many numerical models and remote sensing retrieval algorithms. A fundamental limitation is that cloud and precipitation processes occur on physical scales that are several orders of magnitude smaller than typical cloud-scale model grids or the remote sensing instrument sampling volume. Nevertheless, realistic representation of varied particle populations within clouds is necessary to accurately estimate precipitation rates.

Commonly, a population of particles within some volume is expressed by a particle size distribution (PSD), and weighted integrals (i.e., moments) of the PSD are sensitive to the microphysical evolution of ice-phase particles (Morrison et al. 2020). Ice-phase precipitation mass is proportional to the second moment of the PSD. Because radar reflectivity, Z, is proportional to the square of the mass (i.e., the fourth moment of the PSD), the precipitation mass directly affects power returned to a radar. However, because of the physical complexity arising from diversity in initial ice crystal habits and their unique process-based morphologies with time, assumptions about the particle properties and the PSD are often necessary to derive remote sensing precipitation rate estimates. For example, ice crystals are commonly assumed to be spherical (e.g., Iguchi et al. 2018) and the population may be constrained to a prescriptive PSD shape or snow density (e.g., Grecu et al. 2016). A consequence of such a priori assumptions is that process-based variations cannot be expressed and retrieved precipitation rate estimates are inherently constrained, leading to snowfall rate underestimation and increased error compared to liquid phase (e.g., Speirs et al. 2017). To advance the utility of radar remote sensing measurements of ice-phase precipitation, it is important to understand the quantitative effects of process-based evolution on the intrinsic physical properties of precipitation in natural clouds and their implications for the radar measurements.

A remarkable property of precipitating clouds is that liquid water droplets are frequently present at sub-freezing temperatures alongside ice crystals. A region of cloud containing both ice and sub-freezing (i.e., supercooled) liquid water (SLW) is described as a mixed-phase layer. One implication of the mixed phase particle population is that depositional ice growth occurs at the expense of liquid water due to differences in saturation vapor pressures over ice and liquid

94 surfaces, a process commonly referred to as the Wegener-Bergeron-Findeisen process

95 (Pruppacher and Klett 1997). Additionally, upon contact with falling ice crystals, the SLW

96 droplets freeze and are accreted by the crystal (i.e., riming), initiating a physical morphology of

97 the particle. Natural ice crystals demonstrate tremendous variability in shape and complexity

98 depending on growth habits (e.g., Magono and Lee 1966; Pruppacher and Klett 1997; Bailey and

99 Hallet 2009). Because of this diversity, it is often convenient to define the crystal size along

100 major and minor axes while the major axis is assumed to be along the maximum dimension of

101 the crystal and the minor axis is along an orthogonal orientation. The aspect ratio defines the

102 ratio between the crystal dimensions along the minor and major axes (Jensen and Harrington

103 2015). One commonly adopted conceptual description for the change in particle properties

104 during riming is the "fill-in" model (Heymsfield 1982) whereby the liquid water will initially fill

105 open voids, while largely maintaining the initial dimensions of the crystal axes. During later

106 stages of the "fill-in" riming model, rime accumulates on the underside of the falling crystal,

107 increasing the minor dimension of the crystal while the major dimension remains unchanged.

108 With increasing riming, aspect ratio approaches unity, which is expected for heavily rimed

109 graupel particles. Consequently, riming results in increasing particle density and, therefore, fall

110 velocity. The adjustments in particle geometry and fall characteristics with rime accumulation

111 are relative to, and dependent on, the initial ice crystal geometry and accreted rime but further

112 dependent on prior and concurrent processes including vapor depositional growth and

113 aggregation (e.g., Jensen and Harrington 2015).

114   Ice-phase particle growth by deposition of vapor-phase water directly increases the ice water

115 content (IWC) and therefore, yields direct increases in Z (Field et al. 2005, 2007). However,

116 depositional mass accumulation occurs at a relatively slow rate, thus, gradual increases in Z are

117 expected from depositional growth alone. Aggregation of two or more particles does not

118 explicitly alter the IWC of the particles, but rather redistributes the mass to a larger size particle.

119 Despite unchanging IWC, increased particle diameters, D, during aggregation enhances radar

120 scattering at a rate proportional to D^4 and consequently, Z may be significantly increased by

121 effects of aggregation. Through accumulation of liquid-phase water which yields increases in

122 IWC, similar, rapid adjustments in Z are also possible during riming. Evaluation of process-

123 based effects on the evolution of the PSD moments and their implications for precipitation

124 fallout from natural clouds is challenging because specific processes cannot be readily isolated,

125   even if observations are collected in situ. In general, observationally-consistent numerical

126   modeling simulations are necessary to determine such effects.

127   The physical scales of processes that govern the formation and evolution of falling ice

128   crystals are not resolved by most numerical models. In bulk- and bin-microphysics schemes, ice-

129   phase processes are commonly expressed implicitly through conversion processes whereby

130   precipitation is exchanged among predefined categories (e.g., ice, snow, graupel, hail; Thompson

131   et al. 2004; Morrison et al. 2005). However, prior studies (e.g., Colle et al. 2005; Morrison and

132   Milbrandt 2011; van Weverberg et al. 2012) have demonstrated that the precipitation evolution

133   and fallout is sensitive to a priori thresholds that define category conversions (e.g., snow to

134   graupel during riming). For rimed growth, Lagrangian particle-based model simulations indicate

135   that bulk particle density can undergo rapid evolution in response to small variations in the

136   background SLW concentration, significantly modulating the particle fall velocity and surface

137   precipitation rate (DeLaFrance et al. 2024). For remote sensing retrievals of mixed-phase

138   precipitation, the effects of rime accumulation are constrained by the a priori assumptions about

139   the particle's mass, geometry, or fall characteristics. Recently, diverse methodologies leveraging

140   multi-frequency, dual-polarization, and Doppler radar measurements have been proposed for

141   retrieving some properties of ice-phase particles that would otherwise be prescribed (e.g.,

142   Leinonen and Szyrmer 2015; Kneifel et al. 2016; Moisseev et al. 2017; Oue et al. 2018;

143   Leinonen et al. 2018; Mason et al. 2019, Chase et al. 2021). Among these methods, leveraging

144   radar Doppler data has shown promise in inferring the onset of riming and, subsequently, the

145   riming-based modulations of retrieved particle property estimates. Mason et al. (2018)

146   demonstrated that the addition of Doppler radar measurements provides constraint on the bulk

147   ice density parameter in retrievals of snowfall. Furthermore, as shown by Kalesse et al. (2016),

148   rimed snow occupies a unique region of Doppler spectra distinct from unrimed snow. One-

149   dimensional (1D) spectral bin microphysics modeling simulations have shown promise in

150   reproducing the Doppler spectra moments of riming but demonstrate sensitivity to particle

151   property assumptions (Kalesse et al. 2016).

152   The 1D columnar modeling approach offers a framework for simulating explicit

153   microphysical processes and detailed particle properties that are computationally prohibitive in a

154   three-dimensional (3D) dynamic model. The 1D construction is therefore well suited to advanced

155   bin and Lagrangian particle-based microphysics schemes. One challenge for such simulation

designs, however, is constraining the model in a way that minimizes assumptions and, as a result, ambiguity in the attributing physical process for adjustments in the cloud's radar and precipitation characteristics (e.g., Kalesse et al. 2016; Bringi et al. 2020). Some assumptions can be constrained by coincident in situ and remote sensing radar measurements.

Data collected during winters of 2020, 2022, and 2023 from the Investigation of Microphysics and Precipitation for Atlantic Coast Threatening Snowstorms (IMPACTS) campaign (McMurdie et al. 2022) provide those constraints. Midlatitude cyclones over the United States East Coast and Midwest regions were comprehensively sampled by coordinated aircraft- and ground-based platforms to better understand the precipitation microphysics within regions of snowfall that organize into elongated regions commonly recognized as snowbands (e.g., Novak et al. 2004). Consistent with IMPACTS's goal to support improved numerical modeling and remote sensing retrievals of winter precipitation, in the present study we investigate the process-based effects of riming in a sampled storm that produced moderate rates of wintry-mixed precipitation for a prolonged period over the Northeast. Our overarching approach is to combine these observations with numerical modeling simulations to describe the process-based particle evolution and contributions of riming to the observed radar properties and precipitation rates. Here, we use an observationally-constrained, sophisticated Lagrangian particle-based model within a 1D columnar framework to address the following questions:

1. Can primary ice processes (i.e., deposition, aggregation, riming) within a simplified 1D simulation reasonably reproduce the observed evolution of particles within the natural cloud?
2. What were the quantitative contributions of riming to the observed Doppler radar vertical profiles and to the surface precipitation rate?
3. Do simulated Doppler radar vertical profiles yield characteristic responses to the onset or degree of riming that is distinct from other ice-phase processes (e.g., aggregation)?

2. Winter Storm Observations

2.1. 04 February 2022 Case Study

For this analysis, we will use IMPACTS observations collected during the 04 February 2022 event that delivered wintry-mixed precipitation across a broad region of the northeast US.

187 IMPACTS deployed an in situ (P-3) and remote sensing (ER-2) aircraft. The P-3 aircraft was

188 equipped with instrumentation to measure the in situ cloud microphysical properties and the

189 high-altitude ER-2 aircraft was equipped with nadir-viewing remote sensing instrumentation

190 analogous to those onboard satellite-based platforms (e.g., Skofronick-Jackson et al. 2017). The

191 two aircraft targeted the storm over the coastal New England area where, as an example of the

192 surface precipitation characteristics during this event, the Boston, MA (KBOS) Automated

193 Surface Observing System (ASOS; Brodzik 2022a) reported nearly 32 mm of precipitation in 24

194 hours. Precipitation initially accumulated in the form of light to heavy rain before transitioning to

195 freezing rain at about 1300 UTC, ice pellets by 1600 UTC, and back to freezing rain at about

196 1930 UTC. A transition to snow and continued accumulation occurred on 05 February at KBOS

197 and over most of the New England area.

198   Winter storms that impact the northeast US are commonly described according to the track of

199 the low-pressure center, with implications for their precipitation characteristics. From these

200 tracks, Zaremba et al. (2024) classified twenty-six IMPACTS events in one of six categories,

201 which varied in, for example, rates and regions of cyclogenesis, frontal forcing, and precipitation

202 intensity and distribution. Six of the events were classified as cold fronts and had relatively weak

203 and expansive low-pressure areas which yielded widespread rain and snow along, and extending

204 to the cold side of, the front. As one of these cold front events, the 04 February case had a broad

205 frontal boundary that extended from the Gulf of Mexico to Maine. The prolonged period of

206 wintry-mixed precipitation over the northeast US was sustained by isentropic lifting of moisture-

207 rich low-level flow along this front and overrunning a surface layer which, for many areas,

208 remained subfreezing. Over the eastern US, a mean southwesterly flow developed ahead of an

209 initially positively tilted 250-hPa trough at 0000 UTC 04 February that developed to nearly

210 neutral tilt by 0000 UTC 05 February (Fig. 1a-c). An associated jet streak exceeding 150 kts was

211 situated over northern New England such that between about 1200 UTC 04 and 0000 UTC 05

212 February, upper-level divergence in the right entrance region further supported lifting within the

213 atmospheric column (Bjerknes 1951; Uccellini and Kocin 1987; Holton and Hakim 2012).

214 During this time period, a modest elongated southwest-northeast oriented low-pressure minimum

215 of approximately 1010 hPa was maintained over a broad region of coastal New England (Fig. 1d-

216 f).

217
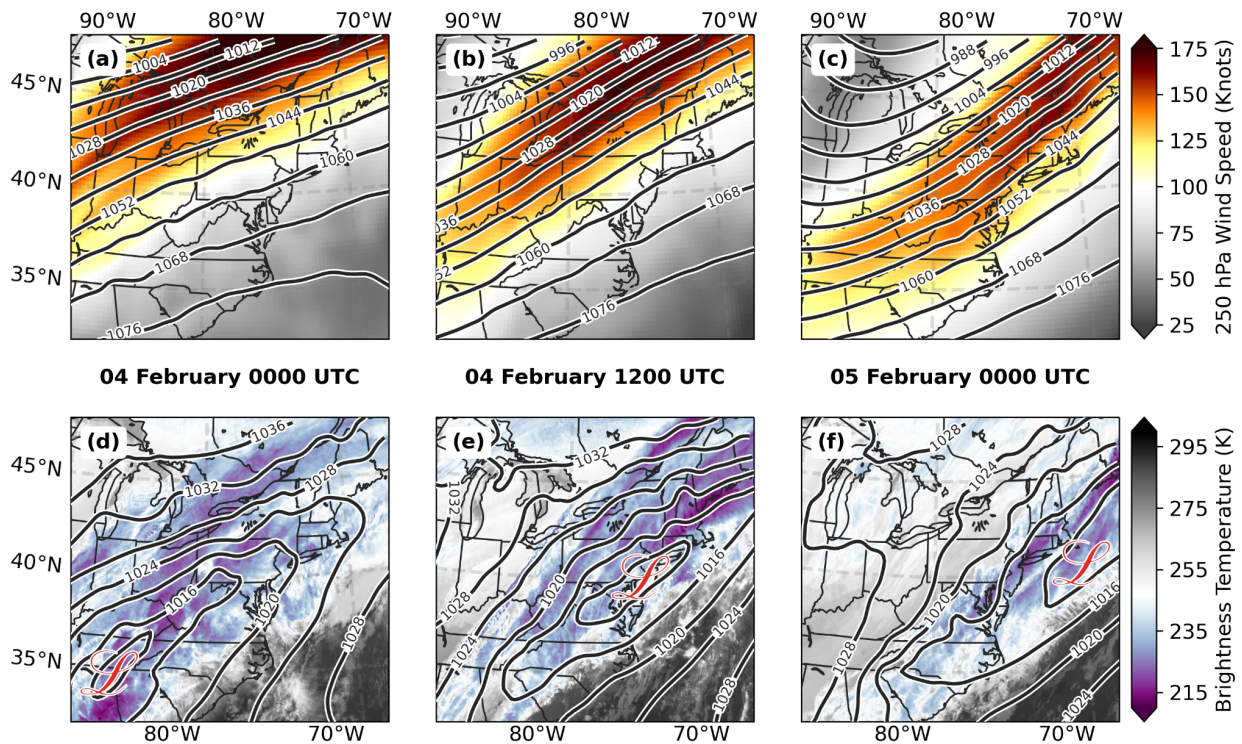
Figure 1: *Synoptic evolution of the winter storm that impacted the northeast US: (a-c) 250 hPa geopotential heights (dam) and wind speeds (knots) and (d-f) mean sea level pressure (MSLP, hPa) and cloud brightness temperature (K) for the times 0000 UTC 4 February (a, c); 1200 UTC 4 February (b, e) and 0000 UTC 5 February 2022 (c, f) . The 250-hPa and MSLP data are from the European Center for Medium-Range Weather Forecast Reanalysis v5 (ERA5; Hersbach et al. 2020) and the brightness temperature data are from the Geostationary Operational Environmental Satellites (GOES) 10.3 µm channel (Brodzik 2022b).*

Between about 1300 and 1800 UTC, the P-3 and ER-2 aircrafts flew a "lawnmower-style" pattern orthogonal to the long axis of an enhanced region of reflectivity while translating subsequent flight legs to the northeast, such that the storm was sampled in an approximately Lagrangian manner (Fig. 2a). The P-3 flew its initial flight leg south to north beginning at about 1340 UTC briefly at 6.5 km MSL before descending to a constant altitude of about 6.2 km MSL. At the southern end, this initial flight leg was near the NWS rawinsonde launch site at Islip, NY (KOKX). The P-3 descended on each subsequent flight leg to sample different layers of the cloud reaching an altitude of 3.0 km MSL on the final north-to-south flight leg, which transected the 0°C melting level. The two enhanced regions of reflectivity, on either side of the surface

237 frontal boundary, exhibited differing cloud and precipitation properties. At the surface, the

238 northern region of enhanced reflectivity was dominated by snowfall whereas the southern region

239 was dominated by rain during the period of aircraft sampling then transitioning to wintry-mixed

240 precipitation. As we describe in Section 2.2, in situ measurements are used to indicate riming,

241 which was commonly observed over the southern region of enhanced reflectivity but absent over

242 the northern region. Therefore, to address our science questions, our present analysis is

243 constrained to measurements of the southern portions of flight legs (Fig. 2a).

244
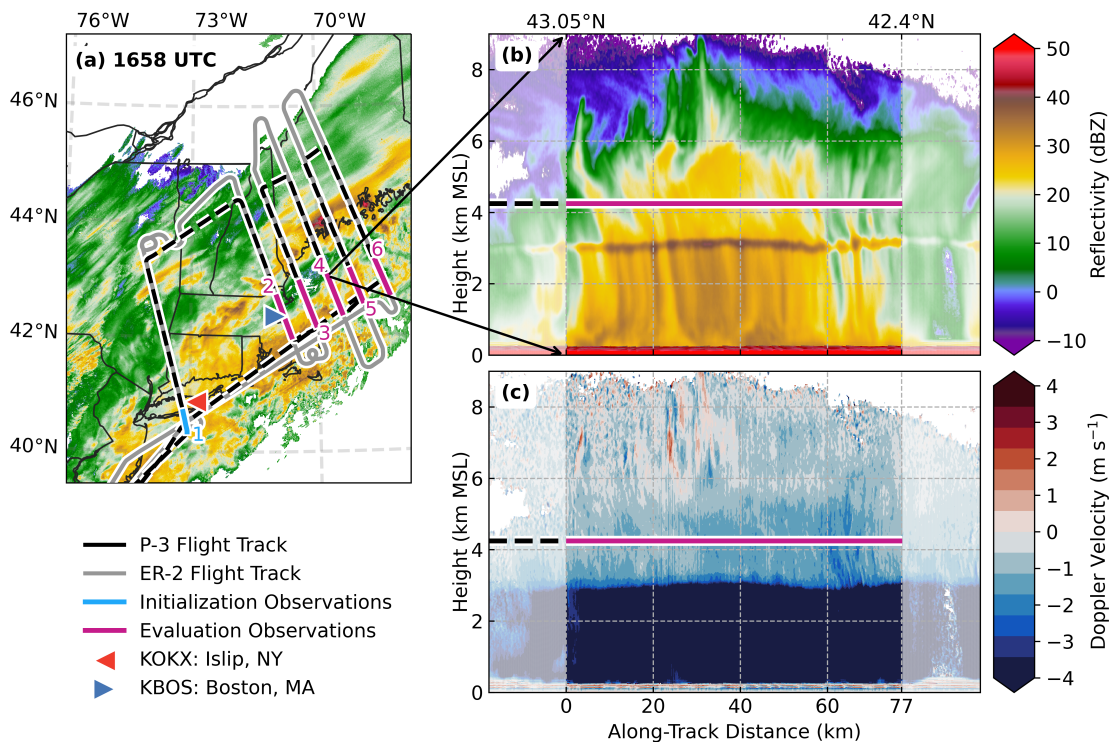
245

246 **Figure 2**: *IMPACTS operations on 04 February 2022 over the northeast US targeting regions of*
247 *enhanced reflectivity that persisted for several hours in the operational National Weather*
248 *Service (NWS) Multi-Radar Multi-Sensor (MRMS; Zhang et al. 2011) product. Shown are (a) the*
249 *coordinated P-3 and ER-2 flight tracks and MRMS composite reflectivity at approximately mid-*
250 *flight (1658 UTC) with subsets for each numbered flight leg at the southern enhanced region of*
251 *reflectivity indicating data used for this study. Also indicated in (a) are the NWS rawinsonde*
252 *launch site at Islip, NY (KOKX) and ground verification site at Boston, MA (KBOS). Ku-band*
253 *reflectivity (b) and Doppler velocity (c) vertical profiles as measured by the ER-2 aircraft from*
254 *1628 (north) to 1634 UTC (south) depict the vertical cloud profile across the region of enhanced*
255 *reflectivity (between transparent regions) for the fourth flight leg while the P-3 aircraft sampled*
256 *in situ at ~4.3 km MSL altitude (magenta line in b, c), ending the flight leg at ~42.4°N.*

257

258

2.2. Observations: Surface Based, Remote Sensing, and In Situ

The initial ER-2 and P-3 flight leg approximately overflew the NWS operational Islip, NY (KOKX) rawinsonde launch site (Fig. 2a). Because of the relatively steady-state nature of the storm during the aircraft sampling period, the KOKX 1200 UTC rawinsonde (Waldstreicher and Brodzik 2022) is used to estimate the atmospheric properties in the southern portion of the flight legs. Because these southern portions of the flight legs were mostly offshore, we use the nearest ASOS measurements at KBOS between 1300 and 1800 UTC to estimate the mean surface precipitation rate for model comparison. The ER-2 aircraft flew well above the storm at approximately 20 km MSL and operated two nadir-viewing radars on 04 February: the dual-band 13.9 GHz (Ku-band) and 35.6 GHz (Ka-band) High-Altitude Wind and Rain Airborne Profiler (HIWRAP; Li et al. 2016; Mclinden et al. 2022a) and the 94 GHz (W-band) Cloud Radar System (CRS; McLinden et al. 2022b). For radar reflectivity and Doppler velocity measurements of the precipitation, we use HIWRAP measurements, which have a vertical resolution of 150 m and a surface footprint of 1 km. At Ku-band, HIWRAP has a minimum sensitivity of approximately -10 dB at an altitude of 10 km MSL (Li et al. 2016).

Of the numerous instruments onboard the P-3 aircraft, those of relevance to this study include cloud Optical Array Probes (OAPs) and those that measure Liquid Water Content (LWC) and vertical air motion. The OAPs provide measurements of the two-dimensional projected sizes, shapes, and concentrations of particles. Data from a Two-Dimensional Stereo (2D-S; Lawson et al. 2006), which is commonly used for measurements of particles smaller than about 1 mm in diameter, are unavailable for the 04 February flight. However, a vertically oriented High-Volume Precipitation Spectrometer (HVPS; Lawson et al. 1993) provided particle measurements at sizes greater than 0.5 mm which were used to construct PSDs. Measurements of LWC were obtained from a Fast Cloud Droplet Probe (FCDP; Lawson et al. 2017) which operated as part of the Hawkeye combination probe. The FCDP uses Mie light scattering principles to size and count liquid water droplets from 2 to 50 μm in diameter, from which number and mass concentrations can be derived. Processing of the OAP and FCDP data was performed by the National Center for Atmospheric Research (NCAR; Bansemer et al. 2022) and is used at a 1 Hz frequency. Vertical air motion measurements were provided by the Turbulent Air Motion Measurement System (TAMMS), which uses several sensors at different locations on the aircraft to estimate the 3D components of the ambient wind (Thornhill et al. 2003). For

290 TAMMS configured to the P-3, the accuracy of vertical winds measurements is estimated to be

291 0.2 m s^{-1} (Thornhill 2022).

292

293 **3. Simulation Design and Validation**

294 **3.1. Model Description**

295 Several bulk microphysics schemes have been developed to more realistically represent the

296 observed continuous evolution of ice-phase particle populations during riming (e.g., Morrison

297 and Milbrandt 2015; Jensen et al. 2017; Cholette et al. 2023). Recently, this modeling approach

298 has been extended to a Lagrangian particle-based scheme in the novel McSnow model (Brdar

299 and Seifert 2018). The particle-based approach affords some advantages over the bulk approach,

300 namely that evolution of a population of particles occurs independent of an Eulerian grid cell

301 structure and is not constrained by assumptions about the PSD. The McSnow model was

302 developed in a 1D columnar configuration and was expressly designed to simulate the evolution

303 of an initial particle population during sedimentation through the column (Brdar and Seifert

304 2018). The notion of a particle in McSnow follows the super-droplet principle (Shima et al.

305 2009) whereby a multiplicity of real particles having commonality among physical properties

306 and location are represented by a single super-particle. These super-particles are continuously

307 introduced in the upper boundary of the model such that initially prescribed PSD characteristics

308 are maintained and then evolve by vapor deposition and aggregation, with an option for riming to

309 occur within a user-defined mixed-phase layer. From 2D simulations using McSnow,

310 DeLaFrance et al. (2024) demonstrated that mixed-phase layer depth significantly modulates

311 surface precipitation rates, varying up to 50% in response to a depth change of 750 m and that in

312 situ measurements of SLW content provide a constraint on the layer's vertical extent. Following

313 riming, melting of the particles occurs as its surface temperature exceeds 0°C, and collision-

314 coalescence processes may then occur, but no additional precipitation mass is generated by

315 warm-rain processes. The thermodynamic profile is prescribed and there are no mechanisms of

316 feedback on the ambient environment based on the microphysical processes.

317 At any point in the column, detailed information about individual particle properties are

318 directly accessible. In general, however, there is greater utility in the description of a population

319 of particles in the form of a binned PSD expressed as the number concentration, N, of particles

320 with diameter, D. We use a construction of 200 bins linearly spaced from 2 μm to 10 cm. From

321 the PSD, radar quantities associated with moments of the PSD are computed by using a forward

322 operator to estimate the radar scattering properties. Several scattering models have previously

323 been adopted to radar scattering from ice crystals, principally differing in the complexity of the

324 scattering particle's geometry. A population of ice crystals may be treated as spheres and

325 scattering computed directly from Mie theory (Bohren and Huffman 1983); however, this

326 approach vastly simplifies the irregular geometry of natural ice crystals. Scattering estimates

327 based on the T-matrix method (Mishchenko et al. 1996) support nonsphericity of particles using

328 a spheroidal shape. Furthermore, the orientation of the spheroids relative to the radar beam may

329 be specified or randomized (Mishchenko and Travis 1998). A more sophisticated approach

330 termed discrete-dipole approximation (DDA) accounts for the complex scattering interactions of

331 irregular crystal geometry (Purcell and Pennypacker 1973) and is therefore a compelling method

332 to estimate scattering of natural crystals. However, for our simulations, crystal habits or detailed

333 properties of particle geometry are not predicted and thus, T-matrix is an apt method of

334 estimating radar scattering. Specifically, we use the PyTMatrix software (Leinonen 2014) to

335 estimate the radar backscattering cross section, σ, and compute Z, defined as:

$$Z = \frac{\lambda^4}{\pi^5 |K|^2} 10^{18} \int_0^\infty \sigma(D) N(D) dD, \tag{1}$$

337 where λ is the radar wavelength and K is the dielectric factor. From the simulations, we also

338 estimate Doppler velocity, V_D, which is the reflectivity-weighted fall velocity, v, of the particles,

339 defined as:

$$V_D = \frac{\int_0^\infty v(D) \sigma(D) N(D) dD}{\int_0^\infty \sigma(D) N(D) dD}. \tag{2}$$

341 For a mixed-phase cloud, Tridon et al. (2019) demonstrated a degradation of skill in T-matrix Z

342 estimates at higher radar frequencies (i.e., Ka- and W-band). To minimize uncertainties

343 associated with non-Rayleigh radar scattering effects (e.g., Matrosov 2007; Liu 2004, 2008), we

344 specify $\lambda = 25$ mm for all calculations, which is comparable to the Ku channel on the HIWRAP

345 radar. Additionally, for consistency with the HIWRAP measurements, a two-way correction for

346 attenuation due to precipitation particles was applied following methodology described in

347 Williams (2022).

348
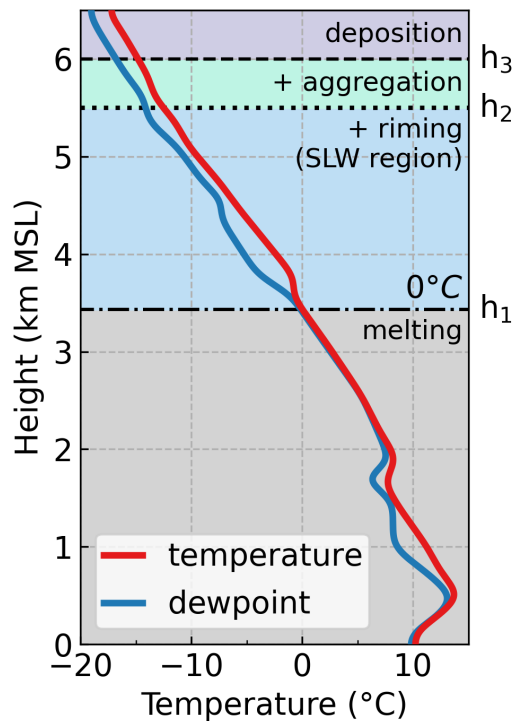
Figure 3: *Schematic of the one-dimensional columnar configuration of the McSnow model with prescriptive process-based layers for evolution of new particles initiated at the column's upper boundary. Static temperature and dew point vertical profiles are derived from the 04 February 1200 UTC KOKX rawinsonde.*

3.2. Control Simulation Design

We use the in situ measurements combined with rawinsonde data to construct a quasi-idealized cloud profile that is representative of the mean state of the 04 February storm which we apply prescriptively in the 1D columnar McSnow model. The process-based model design is illustrated by the schematic in Fig. 3. Introduction of new particles from a prescribed PSD occurs at 6.5 km MSL, which approximately corresponds to the uppermost height of in situ observations. Dominant particle types observed at this height were side planes and bullet rosettes. As newly introduced particles undergo sedimentation, growth occurs initially by vapor deposition only. Aggregation is introduced at 6 km MSL (-15°C) since aggregate particles, mostly side planes and other planar crystals, were present in observations below 6 km MSL. Riming is introduced at 5.5 km MSL, which we approximate as an upper extent of the mixed-phase layer based on the presence of SLW droplets and rimed particles beginning at flight leg 3

368   (4.9 km MSL) and, subsequently, on legs 4 and 5 (4.3 and 3.6 km MSL). The onset of melting is

369   determined by the thermodynamic profile which is obtained from the 1200 UTC KOKX

370   rawinsonde. Although model processes are largely independent of an Eulerian grid (see

371   discussion in Brdar and Seifert 2018, Section 2), model output and analysis occurs on a gridded

372   column with 500 vertical levels, which yields a vertical resolution of 13 m. Additionally, we

373   specify a time step of 5 s and total run duration of ten hours; results are analyzed as averages

374   over the final five hours, after the system has reached a steady state.

375   As a constraint on the observational data used for simulation construction, we approximate

376   the horizontal extent of the southern region of enhanced reflectivity by visually assessing its

377   lateral edges during each flight leg using the Ku-band radar vertical profiles. An example of this

378   approach is provided in Fig. 2b, c for the fourth flight leg in which data used is from the center

379   portion of the figure. The boundaries (opaque regions) varied for each flight leg, adapting to the

380   northeastward progression of the storm and translation of each flight leg. The initial PSD

381   characteristics are derived from an average of the measurements on the uppermost height flight

382   leg at ~6.5 km MSL between the southern end point of the leg and 40.7°N latitude (see Fig. 2a).

383   Because measurements are unavailable for particles smaller than 0.5 mm, we fit a Gamma

384   distribution to the mean PSD from HVPS measurements and then extend the fitted distribution to

385   a lower size limit of 112.5 μm to estimate an IWC of 0.14 g m^{-3} and total number concentration,

386   N, of 23 x 10^3 m^{-3}. For all simulations, an initial super-particle multiplicity of 10^5 in the upper

387   boundary is specified. We assume that newly initialized particles at 6.5 km MSL have a mass-

388   dimension relationship of $m = 0.00294D^{1.94}$ (cgs units) following Brown and Francis (1995), for

389   unrimed aggregate ice crystals in a stratiform cloud. From analysis of four IMPACTS events

390   during the preceding 2020 deployment, Heymsfield et al. (2023) showed that Z calculated from a

391   PSD using the Brown and Francis (1995) mass-dimension relationship and a T-matrix approach

392   yielded an agreement with observations at Ku band within 1.15 dB.

393
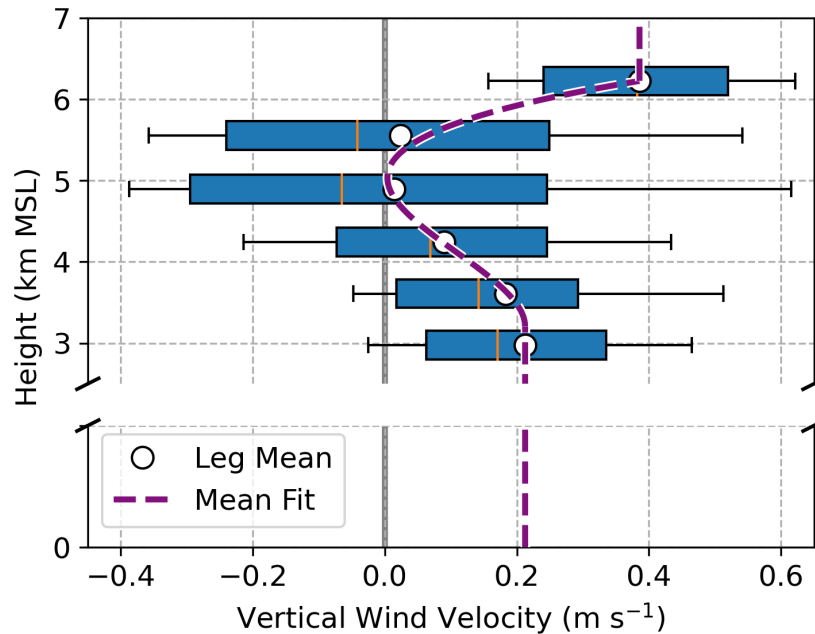
Figure 4: *Vertical wind velocity measurements from the Turbulent Air Motion Measurement System (TAMMS) during P-3 flight legs indicating lower to upper quartiles in the boxed regions, 10th and 90th percentiles at the whiskers, and medians at the vertical lines. A mean profile is fitted to the flight-level mean values (white markers).*

Falling particles are subject to an updraft. We estimate a mean-state vertical wind profile by fitting a third-degree polynomial curve to the mean measurements from each flight leg and extending the upper- and lower-most measurements as a constant value to heights beyond the observation altitudes (violet curve in Fig. 4). Within the mixed-phase layer (h_2 to h_1 in Fig. 3), SLW properties are derived collectively using FCDP measurements on flight legs 3, 4, and 5. We uniformly prescribe the mean values for SLW concentration of 0.05 g m^{-3} (Fig. 5) and a characteristic droplet diameter of 22 μm within the mixed-phase layer.

409
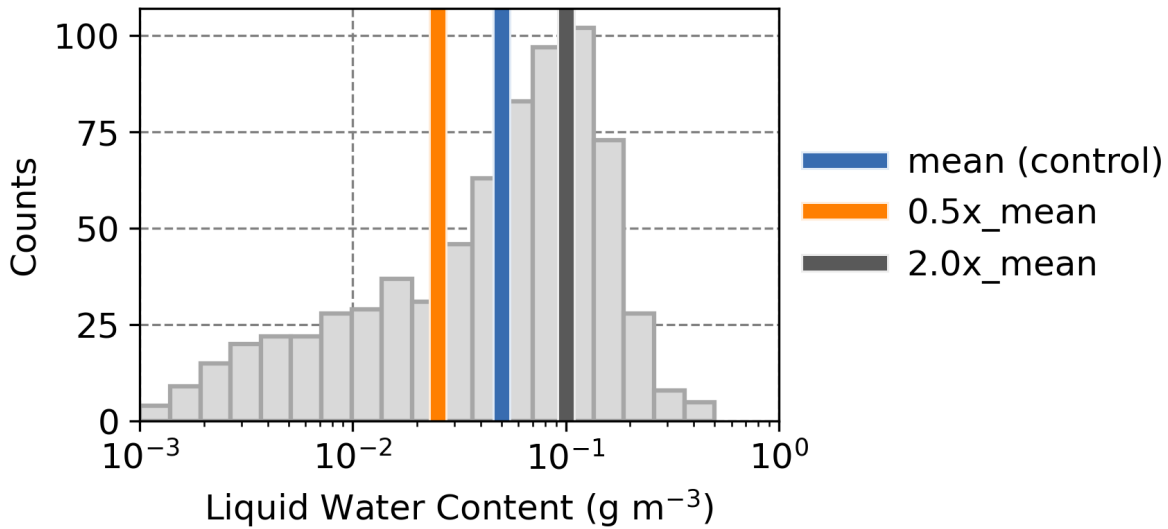
Figure 5: *Histogram of liquid water content (LWC) measurements from the Fast Cloud Droplet*
410 *Probe (FCDP) during P-3 flight legs through mixed phase cloud (4.9 to 3.6 km MSL). Vertical*
411 *bars indicate mean (0.05 g m^{-3}) and perturbed-state values used for sensitivity simulations scaled*
412 *from the mean by factors of 0.5 and 2.0.*
413

414

415

416   Although we prioritize the use of observations for model constraint, several decisions are

417   necessary regarding the parameterizations of modeled processes. With two exceptions, these

418   parameterization decisions follow those discussed in DeLaFrance et al. (2024, see Section 2.3

419   and Appendix A). The first difference regards the aggregation process. Upon collision of two or

420   more particles, a sticking efficiency parameter which scales from 0 to 1 is used to describe the

421   probability of the particles merging, where an efficiency of 1 will always yield a union. The

422   sticking efficiency parameterization follows Connolly et al. (2012), which is dependent on

423   temperature and maximizes at -15°C. In testing, however, we found that the maximum likelihood

424   estimate (MLE) values of Connolly et al. (2012; see Fig. 14b) yielded lower concentrations of

425   large particles than were observed. Alternatively, use of a higher efficiency value inspired by the

426   upper extent of their confidence interval yielded a more observationally-consistent PSD

427   evolution and maximum particle sizes. Therefore, aggregation is introduced at 6 km MSL (Fig.

428   3) with a sticking efficiency of 0.9 at -15°C and linearly decreases to 0.5 at -10°C, remaining

429   constant at 0.5 between -10° and 0°C. The second parameterization decision which differs from

430   DeLaFrance et al. (2024) regards riming where a continuous approach was used in favor of a

431 stochastic approach, although they describe only minor differences between the two approaches.

432 In the present analysis, we find a slightly reduced collection of rime mass using the continuous

433 parameterization when compared to the stochastic parameterization. Applying the continuous

434 parameterization approach, particles accumulate a mean rime fractional mass of 0.49 by the time

435 they reach 3.6 km MSL (flight leg 5, immediately above the melting level), whereas applying the

436 stochastic parameterization, a rime fractional mass of 0.55 is accumulated. Visual assessment of

437 the in situ particle imagery indicated that the stochastic method produces a more observationally

438 consistent riming evolution. Therefore, the stochastic riming parameterization is used in all

439 simulations.

440

441 **3.3. Control Simulation Assessment**

442 The objective for a control simulation is to produce an evolution of a population of particles

443 within a vertical column that is physically consistent with the observed cloud profile. In Fig. 6,

444 we compare the control simulation PSD to the mean observed PSD (D ≥ 0.7 mm). Although PSD

445 measurements at smaller particle sizes are unavailable for this flight, the approximately

446 Lagrangian aircraft sampling yielded a temporally consistent evolution of the PSD at larger sizes.

447 Measurements from flight leg 1 are used to assess the simulation during the particle initialization

448 stages within the uppermost region of the model, whereas measurements collected downstream

449 on flight legs 2 through 6 are used to assess simulation performance during the later stages of

450 particle evolution. The model produces an initial particle population at 6.5 km MSL (Fig. 6a) that

451 is consistent with the mean observations at large particle sizes and follows the assumed Gamma

452 distribution form at small sizes. Flight leg 5 (Fig. 2a), at approximately 3.6 km MSL, was the

453 lowest altitude flown before reaching the melting level. At this altitude, evaluation of the

454 simulation shows skill in evolving this initial particle population by deposition, aggregation, and

455 riming processes throughout a nearly 3 km-deep cloud layer.

456 Particle growth between 6.5 km (Fig. 6a) and 3.6 km MSL (Fig. 6b) through aggregation and

457 to a lesser extent, depositional growth, is expressed in the shift of the observed PSD to larger

458 particle sizes. This evolutionary characteristic is reproduced by the control simulation although

459 slightly larger maximum particle sizes are generated, and the ice mass may be underrepresented

460 among particles smaller than about 2 mm in diameter. We note, however, that sizing uncertainty

461 in the observed measurements is greater at these small sizes owing to the relatively coarse pixel

 resolution of 150 μm for the HVPS probe (Bansemer et al. 2022). To further validate the control

463 simulation and to assess the continuous particle evolution throughout the vertical profile, Z is

464 estimated from the simulated PSD and compared to the HIWRAP Ku-band measurements.

465
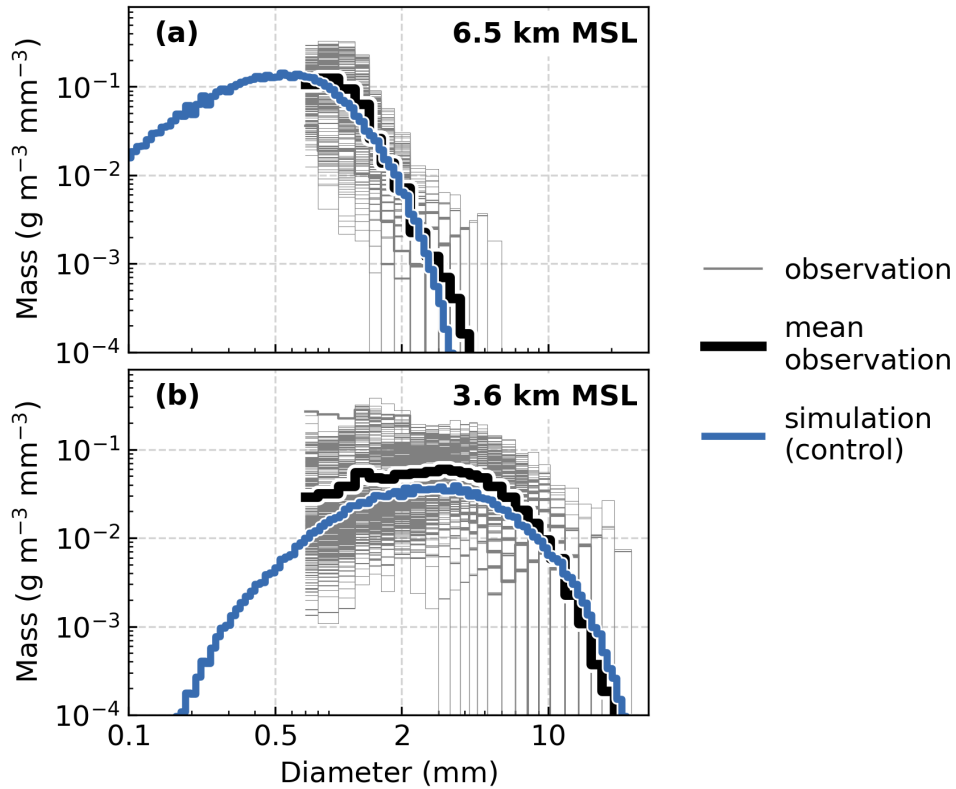
466

467 **Figure 6:** *Particle size distributions (PSDs) of ice mass for observed 1 Hz and mean values*
468 *derived from (a) P-3 flight leg 1 at 6.5 km MSL and (b) flight leg 5 at 3.6 km MSL (see Fig. 2)*
469 *and for the control simulation at equivalent altitudes.*

470

471

472 Figure 7 shows the median observed vertical profile of Z and V_D computed from the

473 downstream flight legs 2 through 6, as indicated in Fig. 2a. Data from the lowest 500 m were

474 removed due to noise from ground clutter. From the observed vertical profiles, several inferences

475 are made about the microphysical processes. Beginning at 6 km MSL, Z rapidly increases with

476 descent, which is expected with an onset of aggregation. The rate of increase in Z with

477 descending height reaches a relative maximum near 5.5 km MSL (Fig. 7a), coincident with an

478 apparent acceleration of V_D. Within the subsequent 1 km (5.5 km to 4.5 km MSL), V_D becomes

479 increasingly negative (-0.72 m s⁻¹ to -1.00 m s⁻¹) as particle fall speeds increase (Fig. 7b). This

480 effect is assumed to be associated with the onset of riming, and subsequently, changes in particle

481 densities. Particle melting begins near 3.4 km MSL, at which point a bright band signature is

482 apparent and V_D rapidly accelerates. Below the bright band, Z remains nearly constant at about

483 25 dBZ and V_D is about -5 m s⁻¹.

484
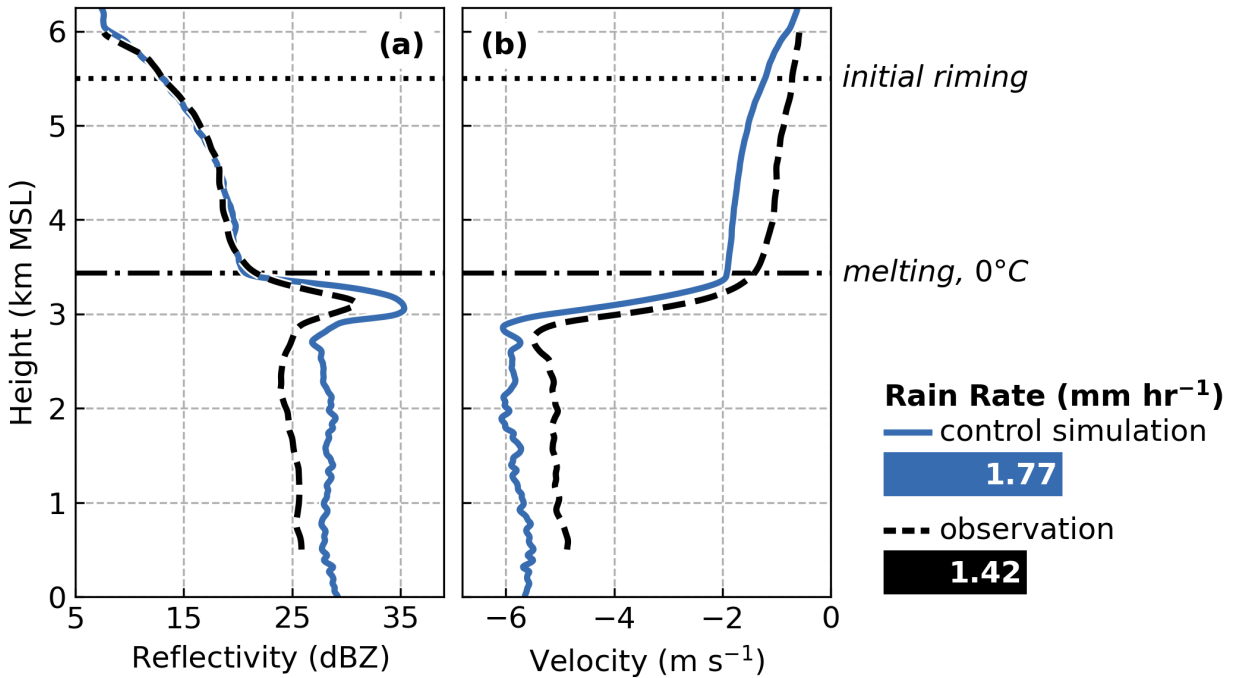
485

486 **Figure 7:** *Vertical profiles of (a) radar reflectivity and (b) Doppler velocity at Ku band for the*
487 *control simulation (blue lines) and observed (dashed black lines) median from ER-2 HIWRAP*
488 *radar during flight legs 2-6 (see Fig. 2a, magenta segments). Data for the observed profile below*
489 *500 m MSL are omitted due to ground clutter. A dotted line at 5.5 km MSL indicates the onset of*
490 *riming and a dash-dotted line indicates the 0°C height. Also shown at the right are the surface*
491 *rain rate values from the control simulation (blue) and observed at KBOS (black) between 1300*
492 *and 1800 UTC on 04 February 2022; horizontal bar lengths illustrate magnitude differences.*
493

494

495 The vertical profile of Z is well reproduced by the control simulation, particularly above the

496 melting level (Fig. 7a), which suggests confidence in its prescriptive configuration. Upon

497 melting, Z is overestimated by the control simulation and maintains a bias of about 2 to 5 dB

498 throughout the warm layer. While an evaluation of warm-rain processes is beyond the scope of

499 the present study, it is possible that this overestimate in Z results from an incomplete

500   representation of warm-rain processes by the model, such as droplet breakup and shedding, or

501   from uncertainties in the scattering estimates. Confirmation of an attributable mechanism would

502   be challenging without in situ observations below the melting level. Rain rates at the surface are

503   one common model validation metric. Because the aircraft sampling occurred primarily offshore

504   (see Fig. 2a), an ideally situated ground site is unavailable. However, we find comparison with a

505   nearby ground site useful towards determining whether the control simulation produces

506   physically realistic estimates that are representative of the rainfall across the broader region. At

507   the surface, during aircraft sampling (1300 to 1800 UTC), the nearest ground site, KBOS,

508   reported a rain rate of 1.42 mm hr^{-1}. The control simulation produces about 25% more surface

509   rain with an average rain rate of 1.77 mm hr^{-1}.

510   Despite the confidence in Z aloft, we find that V_D is underestimated by about 0.5 to 1 m s^{-1} in

511   the control simulation but within an uncertainty range of $\pm$ 1 m s^{-1} (Matthew McLinden, personal

512   communication, 25 April 2024) for the HIWRAP Ku-band V_D measurements. Some of the

513   uncertainty in the V_D measurements is due to corrections necessary for the aircraft motion,

514   which, although unlikely to significantly affect the relative evolution of V_D with height, may

515   yield an absolute magnitude bias. This bias between the observed and simulated V_D is consistent

516   throughout the column, suggesting that this consistent bias may be explained, to a large extent,

517   by those uncertainties in the observations. More importantly for this analysis, the relative

518   changes in V_D with height, which have process-based implications, are similar between the

519   observed and simulated profiles.

520

521   **4. Process-Based Contributions and Sensitivities on Doppler Radar Vertical Profiles**

522   A principal advantage of the particle-based design of the McSnow model is that information

523   about microphysical properties is retained by the model at the scale of the individual particles.

524   For particles in the control simulation, the onset of riming at 5.5 km MSL (h_2 in Fig. 3) initiates a

525   change in the physical evolution of the particle with subsequent sedimentation. At 3.6 km MSL,

526   the particles have accumulated a mean rime fractional mass of 0.55, increasing the total

527   precipitation mass and accelerating its fallout rate. Radar scattering by the particle, expressed

528   through Z, is also modified by rime accumulation, yet these effects are difficult to distinguish

529   from concurrent processes, including deposition and aggregation. To investigate these scattering

530   implications, we estimate the vertical profile of Z with and without contributions of rime mass.

531

532
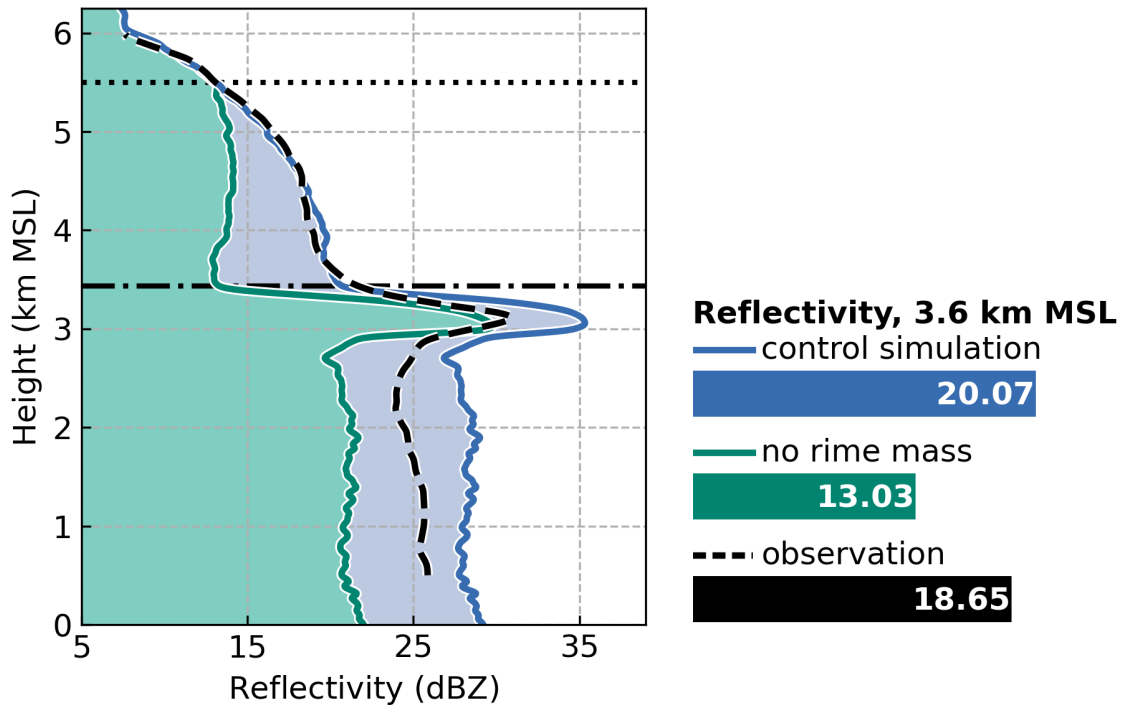
Figure 8: *As in Fig. 7a but with an added vertical profile (in green) for estimated reflectivity (Z) with particle rime mass removed. Shown at the right are simulated and observed Z values computed at 3.6 km MSL; horizontal bar lengths illustrate magnitude differences.*

536

537

Figure 8 compares *Z* from the control simulation (as in Fig. 7a) to an unrimed estimate of *Z* obtained by subtracting the rime mass from the particles and recomputing their scattering properties. Removal of rime mass appears to significantly impede further increases in *Z* with descending height below 5.5. km MSL. Near the melting level, *Z* is reduced from 20.07 to 13.03 dBZ between the control and simulation and the unrimed estimate, suggesting that the accumulated rime mass contributes to about 35% of the total *Z* (in dB units). This calculation, however, only considers the implications of riming on radar scattering; the complex interactions of concurrent processes are neglected by solely removing the rime mass from evolved particles in the control simulation. Additionally, the effects on V_D, which manifest cumulatively during riming, cannot be investigated in the same manner. To explicitly investigate the effects of riming on the radar profiles, and to distinguish these effects from concurrent processes, we introduce several sensitivity simulations which independently perturb the riming or aggregation processes.

550

Simulation	Description	Perturbation Assignment
control	Observation-based **mean-state** simulation	none
high_SLW	**Increase SLW** by **2.0** from control	0.100 g m^{-3} LWC
low_SLW	**Reduce SLW** by **0.5** from control	0.025 g m^{-3} LWC
no_riming	**Remove riming** to distinguish effects from aggregation	Riming process turned off
MLE_C12_agg	**Reduce aggregation** from control to **moderate** efficiency	MLE sticking efficiency; see Fig. 14, Connolly et al. (2012)
low_C12_agg	**Reduce aggregation** from control to **low** efficiency	0.5 x MLE sticking efficiency; see Fig. 14, Connolly et al. (2012)

551

552 **Table 1:** *Descriptions and perturbations relative to the control simulation applied for each*
553 *simulation.*
554

555

556 Although the southern regions of the 04 February 2024 event were predominantly stratiform,

557 variations in the mixed-phase layer LWC were observed (Fig. 5). Within sufficiently deep

558 mixed-phase layers, prior model simulations have demonstrated that small (e.g., < 0.05 g m^{-3})

559 perturbations in LWC alter particle fallout characteristics which can yield substantial increases or

560 decreases in the surface precipitation rate (DeLaFrance et al. 2024). Here, we similarly introduce

561 two sensitivity simulations perturbing LWC within the mixed-phase layer (h_1 to h_2 in Fig. 3),

562 within the range of observed LWC (Fig. 5). In the control simulation, we prescribed the mean

563 observed LWC value of 0.05 g m^{-3}. A scaling factor of two relative to the control is used to

564 prescribe a high concentration (0.1 g m^{-3}) for the "high_SLW" simulation and low concentration

565 (0.025 g m^{-3}) for "low_SLW" concentration. As a limiting case which is analogous to the

566 removal of rime mass (Fig. 8), we construct a "no_riming" simulation with the riming process

567 inactive. A brief summary of these riming sensitivity simulations is provided in Table 1.

568
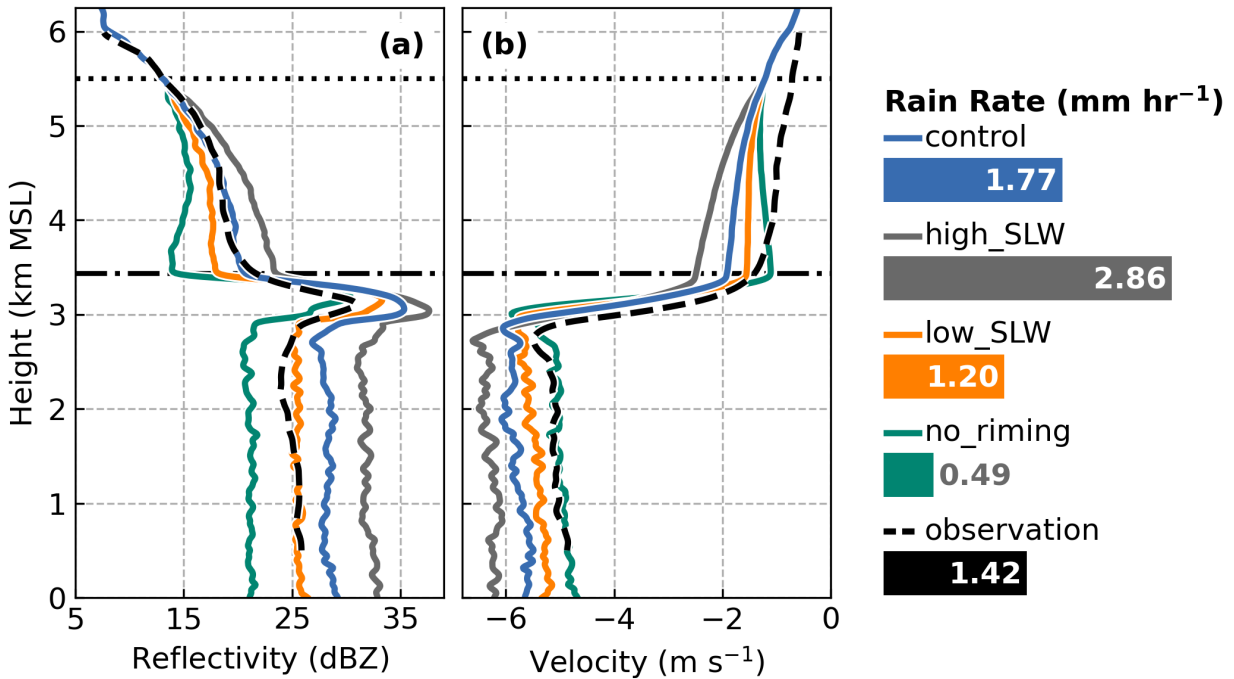
Figure 9: *As in Fig. 7 but for the control and riming-based sensitivity simulations: high_SLW, low_SLW, and no_riming. At the right are surface simulated and observed surface rain rate values; horizontal bar lengths illustrate magnitude differences.*

Vertical profiles of Z and V_D for the high_SLW, low_SLW, and no_riming sensitivity simulations relative to the control are shown in Fig. 9. Complete removal of the riming process in the no riming simulation (Fig. 9a) produces a similar Z profile as found by computing Z for equivalent unrimed particles from the control simulation (Fig. 8). This result underscores the significant sensitivity of Z to changes in particle mass during riming, despite concurrent microphysical processes. Perturbing LWC by a factor of 2 in the high_SLW or 0.5 in the low_SLW simulations relative to the control produces opposing, but similar in magnitude, changes in Z (Fig. 9a), indicating a regularity in the response of Z to SLW variability. Similarly, the effects of SLW variability on V_D demonstrate a regular response (Fig. 9b). We note that these simulation responses in Z and V_D to SLW variability assume that the particles are well mixed such that probabilistic collision of ice crystals and SLW droplets is the same throughout the layer.

As discussed in Section 3.3, remote sensing measurements of V_D, including those from the HIWRAP radar used throughout this study, are subject to magnitude biases. Nonetheless, as with

589   Z, the relative magnitude changes in V_D with height demonstrate a sensitivity to the riming

590   process. In the high_SLW simulation, the rate of further V_D acceleration with descent below 5.5

591   km MSL is nearly doubled relative to the control. Conversely, below about 5 km MSL, further

592   increases in V_D cease in the low_SLW simulation and decrease in V_D occurs in the no_riming

593   simulation. As a result of rime accumulation in the control simulation, V_D immediately above the

594   melting level (3.6 km MSL) increased by about 68% relative to the no_riming simulation.

595   Similarly, Z increased by about 44%. The competing effects of riming and aggregation processes

596   on V_D manifest in the low_SLW and no_riming simulations; riming accelerates the V_D with mass

597   accumulation whereas in the absence of riming, further aggregation yields larger, lower density

598   particles with reduced fall speeds. Consequently, vertical profiles of V_D may provide an insight

599   into dominant microphysical processes, which is consistent with the notion that rimed particles

600   occupy a distinct region of the Doppler spectra (Kalesse et al. 2016). To advance the

601   differentiation of particles evolved by riming, it is necessary to first consider relative effects of

602   variability in the aggregation process.

603   In our development of the control simulation for the 04 February 2022 event, the aggregation

604   process was initially assumed to follow a temperature dependent sticking efficiency identified as

605   the MLE by Connolly et al. (2012; see Fig. 14b). Comparison with in situ PSDs indicated that

606   the MLE sticking efficiency parameter was insufficient to generate observed concentrations of

607   large particles, motivating the use of an increased sticking efficiency in the control simulation.

608   However, to elucidate the effects of aggregation efficiency on radar profiles, we now consider a

609   sensitivity simulation, "MLE_C12_agg", which follows the MLE sticking efficiency of Connolly

610   et al (2012). Additionally, analogous to the design of the riming sensitivity simulations, we

611   introduce a "low_C12_agg" simulation for which the sticking efficiency is further reduced from

612   the MLE estimate by a factor of 0.5. Relative to the control simulation, the reduction in sticking

613   efficiently in the MLE_C12_agg and low_C12_agg sensitivity simulations lack observational

614   consistency with the presently analyzed 04 February 2022 event. However, it is useful to

615   consider the implications of a realistic range of variability in the aggregation process efficiency

616   to inform general distinctions from the effects of riming within vertical profiles of Z and V_D.

617

618
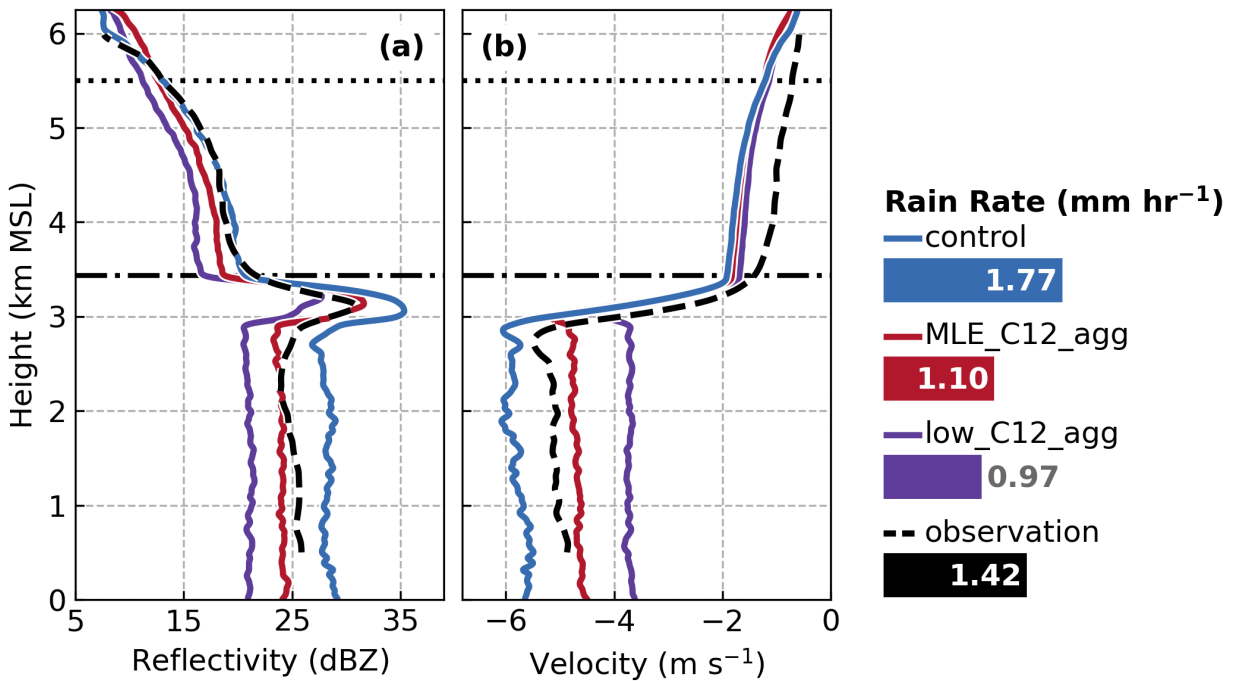
Figure 10: *As in Fig. 7 but for the control and aggregation-based sensitivity simulations:*
MLE_C12_agg, and low_C12_agg. At the right are surface simulated and observed surface rain
rate values; horizontal bar lengths illustrate magnitude differences.

Figure 10 shows the vertical profiles of Z and V_D for the aggregation efficiency sensitivity

simulations, MLE_C12_agg and low_C12_agg. Reducing aggregation efficiency suppresses the

generation of large particles and because of the strong dependency of radar backscatter on

particle size, Z decreases relative to the control (Fig. 10a). Additionally, smaller aggregate

particles become smaller targets for collision with SLW droplets to accumulate rime mass, which

also reduces Z. The latter effect manifests in the reduced surface rain rates, decreasing by 38% in

the MLE_C12_agg (1.10 mm hr^{-1}) and 45% in the low_C12_agg (0.97 mm hr^{-1}) simulations

relative to the control (1.77 mm hr^{-1}). Conversely, a reduction in aggregation efficiency has a

minimal effect on V_D for ice-phase particles (Fig. 10b). Above the melting level, at 3.6 km MSL,

V_D in the MLE_C12_agg simulation is reduced from the control simulation by about 4% and in

the low_C12_agg, reduced by about 13%. This relative insensitivity of V_D to aggregation arises

despite these sensitivity simulations assessing a broad range of possible sticking efficiencies. For

example, at -15°C, the sticking efficiency is reduced from 0.9 in the control to 0.32 in the

637   low_C12_agg simulation and at -10°C, from 0.5 in the control to 0.12 in the low_C12_agg

638   simulation.

639   Below the melting layer, however, the effects of aggregation on V_D become significant,

640   decreasing by approximately 2 m s^{-1} between the control and low_C12_agg simulations.

641   Similarly, the surface rain rate decreases by about 45% between the control and low_C12_agg

642   simulations. Thus, despite the significant implications of the aggregation process on precipitation

643   production and its fallout, its variations are not readily perceived in vertical profiles of V_D. This

644   finding significantly differs from the robust sensitivity of V_D to variations in the riming process.

645   While variations in the aggregation and riming processes may manifest similarly in vertical

646   profiles of Z, we find that V_D is uniquely sensitive to riming. Thus, vertical profiles of V_D show

647   promise in identification of riming as a dominant ice-phase microphysical process, which is

648   ambiguous in profiles of Z, only.

649

650   **5. Discussion**

651   Sensitivity in vertical profiles of both Z and V_D owing to rime accumulation rates were

652   previously shown by Kalesse et al. (2016) from bin model simulations by prescribing a fixed

653   vertical profile of LWC then testing two different riming efficiency parameterizations. Their two

654   simulations yielded similar vertical gradients in Z and V_D profiles but with differences in

655   magnitude. They attributed these differences to assumptions about the physical morphology of

656   the ice crystals with accretion of rime mass that had implications for their scattering properties.

657   In our study, we uniquely provided an observational constraint to establish a control state

658   simulation and modeling framework for assessing impacts of riming and aggregation

659   independently. By selecting a fixed riming parameterization for all simulations using this

660   framework, we were able to assess Z and V_D sensitivities attributable to LWC perturbations

661   within the range of observed variability. We found that a small (≤ 0.05 g m^{-3}) range of

662   perturbations in the LWC produced substantial changes in the surface precipitation rate and a

663   corresponding sensitivity in vertical profiles of Z and V_D.

664   The sensitivities expressed in Doppler radar profiles to LWC perturbations is tied to the

665   impact on bulk microphysical properties, especially particle density, ρ_e. In the deposition- and

666   aggregation-prescribed region above 5.5 km MSL (Fig. 11), ρ_e rapidly decreases with

667   descending height due to the efficient aggregation of increasingly open particle geometry. At 5.5

668   km MSL, riming is introduced and ρ_e approaches 0.02 g cm^{-3}, remaining nearly constant until the

669   melting level as a result of the competing effects of aggregation and riming. In the high_SLW

670   simulation, the effects of riming dominate whereby the gradient in ρ_e abruptly increases with

671   descending height. Conversely, in the low_SLW and no_riming simulations, the effects of

672   aggregation continue to dominate and ρ_e further decreases.

673
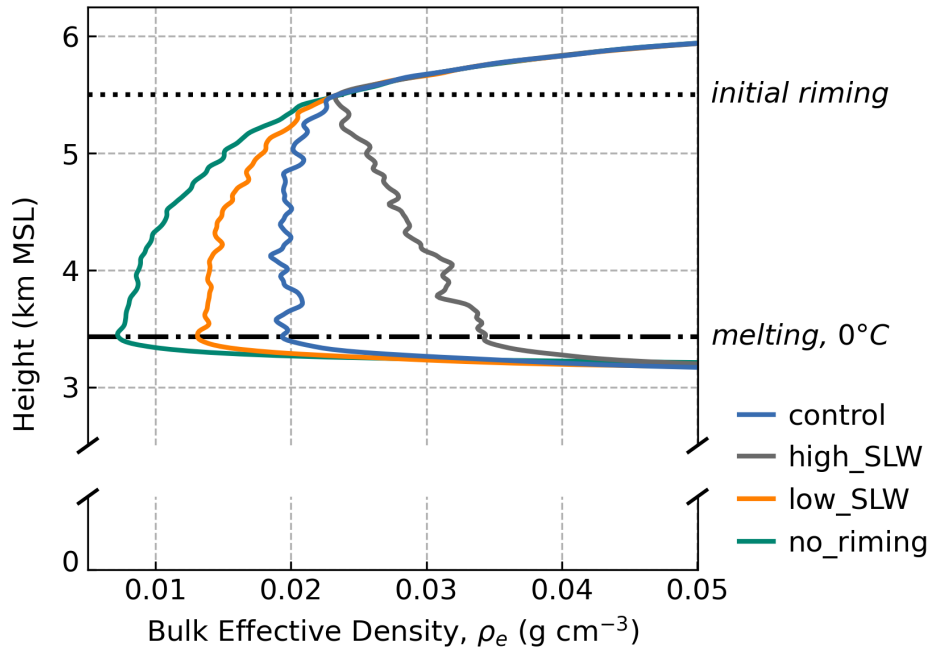
675   **Figure 11:** *Vertical profiles of bulk effective density, ρ_e, for the evolved particle population for*
676   *the control simulation and three riming-based sensitivity simulations described in Section 4:*
677   *high_SLW, low_SLW, and no_riming. Calculations of ρ_e assume equivalent spherical volumes of*
678   *the particles following Heymsfield et al. (2004).*

679

680

681   Despite the opposing process-based effects on the evolution of ρ_e with height, our

682   simulations suggest that the effects of aggregation and riming are not readily distinguished by Z

683   from a Ku-band radar band alone. Riming may be detectable, however, from three-wavelength

684   (Ku-, Ka-, and W-band) radar by leveraging differential attenuation effects. In prior idealized

685   modeling simulations for rimed particle growth scenarios, Leinonen and Szyrmer (2015)

686   identified unique signatures of riming by comparing dual-wavelength ratios (DWR) between Ka

687   and W bands with DWR at Ku and Ka bands. However, they found the magnitude of this

688   signature to be modest and proposed that it would likely be difficult to accurately distinguish in

689 observational data. Mason et al. (2019) later investigated the use of triple-frequency Doppler

690 radar measurements from mixed-phase clouds during wintertime snow events to constrain the

691 retrievals of bulk microphysical properties, including the PSD shape factor and ρ_e. They found

692 that triple-wavelength Z measurements effectively constrained the PSD shape parameter, but did

693 not constrain ρ_e. Rather, V_D measurements were necessary to identify transitions to rimed growth

694 cloud regions and provide constraint on ρ_e. Our findings demonstrate that this constraint on ρ_e is

695 attributable to the unique density-dependent response in V_D expressly owing to variations in the

696 riming process within mixed-phase cloud layers with concurrent riming and aggregational

697 growth. Further, our findings suggest that, when combined with Z, coincident vertical profiling

698 measurements of V_D have utility towards diagnosing riming as a dominant process within

699 stratiform clouds from a single-wavelength radar.

700

701 **6. Conclusions**

702   The evolution of ice-phase precipitating particles within a mixed-phase stratiform cloud was

703 simulated to evaluate the effects of riming on the PSD moments and assess the process-based

704 implications on Doppler radar vertical profiles. In situ and remote sensing airborne observations

705 collected during the IMPACTS field campaign for a prolonged wintry-mixed precipitation event

706 over the northeast US on 04 February 2022 were used to design and constrain a quasi-idealized

707 1D mean-state control simulation. Using the Lagrangian particle-based McSnow model, we

708 defined an initial population of ice particles based on in situ measurements in the upper portion

709 of the cloud. As those particles fell, initial evolution occurred by vapor deposition followed by

710 subsequent additions of aggregation and then riming within prescriptive observation-based

711 layered regions. Radar scattering properties were estimated using a T-matrix forward operator

712 and vertical profiles of Z and V_D were computed from the evolved PSD, then evaluated through

713 comparisons with the airborne radar data. The effects of riming on PSD moments expressed

714 through Z and V_D were assessed from simulations which introduce small perturbations in cloud

715 LWC within a range of observed variability. To distinguish effects of riming and aggregation,

716 two additional sensitivity simulations were introduced to determine the unique implications of

717 aggregational growth efficiency on Z and V_D. Through these approaches, we found:

718

- Ice-phase precipitation particle evolution in a mixed-phase wintertime storm cloud is well constrained by the 1D quasi-idealized McSnow model.
- Despite modest supercooled liquid water concentrations, rime accumulation is estimated to account for 55% of particle mass generated above the melting level, dominating ice-phase contribution to precipitation rates.
- Riming cumulatively increased radar reflectivity above the melting level by an estimated 44% and Doppler velocity by 68% and demonstrated significant sensitivity to small perturbations in supercooled liquid water concentrations.
- Vertical profiles of radar reflectivity demonstrate similar sensitivities to riming and aggregation, but Doppler velocity is uniquely sensitive to riming-based perturbations through changes in particle density.

Constraining parameterized treatments of rimed particle evolution in numerical models is a known source of uncertainty in simulations of precipitation from bulk-, bin- and Lagrangian particle-based models (e.g., Lin and Colle 2011; Jensen and Harrington 2015; Jensen et al. 2017; Brdar and Seifert 2018). One objective of our analysis was to address this constraining need through quantifying precipitation sensitivities to riming in model simulations based on an observed range of variability in LWC. We found a difference of about 6% in rime fractional mass accumulation in our control simulation whether using a continuous or a stochastic representation of riming with the McSnow model. This effect was expressed within a modeling framework using a quasi-idealized and steady-state 1D column with a homogeneous mixed-phase layer. This approach was appropriate for our intentionally selected region of the observed storm because of its idealistic layered vertical structure apparent in radar observations (Fig. 2b, c), along with its known presence of SLW based on in situ observations. However, in reality, processes are not neatly initiated at distinct levels (e.g., in convective areas). It is expected that increasing ambiguity exists in distinguishing concurrent microphysical processes in these scenarios and, thus, our analysis did not assess the full natural range of complexity in mixed-phase precipitation processes.

While model schemes have become increasingly sophisticated, it is not clear that uncertainty in ice-based precipitation estimates have necessarily reduced, highlighting the need for judicious use of observations to advance constraints on modeled processes (e.g., Morrison et al. 2020).

750 Because of the capacity for explicit process representation at the scale of individual particles,

751 Lagrangian models (e.g., McSnow) may be ideally suited to addressing these challenges,

752 especially when combined with datasets which prioritize observations that are consistent with the

753 evolution of particles. This observational consideration was favored during the 04 February 2022

754 event, which was sampled by IMPACTS in an approximately Lagrangian manner. In this study,

755 we focused on riming as a primary ice-phase process, but the northern region of the sampled

756 storm observed significantly less SLW and rime accumulation, presenting a unique natural

757 laboratory for evaluation of modeled aggregation. Sticking efficiencies during aggregation are

758 highly uncertain and difficult to constrain from laboratory experiments (e.g., Connolly et al.

759 2012) yet, as we demonstrated in our study, have significant implications for the accuracy of

760 simulated Z and rain rates. Ongoing work involves curating the in situ measurements of particle

761 evolution within this northern storm region to constrain Lagrangian particle-based simulations

762 and assess the ambient environmental dependencies (i.e., temperature, water supersaturation) and

763 ranges of sensitivities associated with modeled aggregation.

764

765

7. Data Availability Statement

767 All field observation data from IMPACTS used in this study are accessible through the

768 NASA Distributed Active Archive Center (McMurdie et al. 2019). Readers can find a complete

769 description of the McSnow model and its availability in Brdar and Seifert (2018).

770

8. Author Contributions

772 All authors contributed to the study design and methodology decisions. Andrew DeLaFrance

773 conducted the data curation and performed the simulations and computations from model output.

774 All authors contributed to the evaluation and interpretation of the results. Andrew DeLaFrance

775 prepared the manuscript with contributions from all co-authors.

776

9. Competing Interests

778 The authors declare that they have no conflict of interest.

779

780

10. Acknowledgments

The authors acknowledge the entire IMPACTS team for their excellence in the collection and distribution of the robust IMPACTS dataset. The authors thank Axel Seifert and Christoph Siewert for their support and feedback regarding application of the McSnow model. The authors also expressly thank Aaron Bansemer for processing of the microphysics probe data and helpful discussions regarding its application and limitations. Funding was provided by NASA Future Investigators in NASA Earth and Space Science Technology Grant # 80NSSC21K1589 and NASA Grant # 80NSSC19K0338. NCAR provided resources for Andrew DeLaFrance to visit its Mesoscale and Microscale Meteorology Laboratory (host Andrew Heymsfield), which benefited the design and data curation for this analysis. Andrew Heymsfield is supported by the IMPACTS field program under NASA Grant # 80NSSC19K0397 and by the National Science Foundation. We are grateful for the feedback received from two anonymous reviewers, which greatly improved this manuscript.

11. References

Bailey, M. P. and Hallett, J.: A Comprehensive Habit Diagram for Atmospheric Ice Crystals: Confirmation from the Laboratory, AIRS II, and Other Field Studies, J. Atmos. Sci., 66, 2888–2899, https://doi.org/10.1175/2009JAS2883.1, 2009.

Bansemer, A., Delene D., Heymsfield A., O'Brien J., Poellot M., Sand K., Sova G., Moore J., and Nairy, C.: NCAR Particle Probes IMPACTS, Dataset available online from the NASA Global Hydrometeorology Resource Center DAAC, Huntsville, Alabama, U.S.A., https://doi.org/10.5067/IMPACTS/PROBES/DATA101, 2022.

Bjerknes, J.: Extratropical Cyclones, in: Compendium of Meteorology, edited by: Malone, T. F., American Meteorological Society, Boston, MA, 577–598, https://doi.org/10.1007/978-1-940033-70-9_48, 1951.

Bohren, C. F. and Huffman, D. R.: Absorption and Scattering of Light by Small Particles, John Wiley and Sons, New York, 530 pp., ISBN 3527618163, 1983.

Brdar, S. and Seifert, A.: McSnow: A Monte-Carlo Particle Model for Riming and Aggregation of Ice Particles in a Multidimensional Microphysical Phase Space, J. Adv. Model Earth Sy., 10, 187–206, https://doi.org/10.1002/2017MS001167, 2018.

Bringi, V., Seifert, A., Wu, W., Thurai, M., Huang, G.-J., and Siewert, C.: Hurricane Dorian Outer Rain Band Observations and 1D Particle Model Simulations: A Case Study, Atmosphere, 11, 879, https://doi.org/10.3390/atmos11080879, 2020.

Brodzik, S.: Automated Surface Observing System (ASOS) IMPACTS, Dataset available online from the NASA Global Hydrometeorology Resource Center DAAC, Huntsville, Alabama, U.S.A., https://doi.org/10.5067/IMPACTS/ASOS/DATA101, 2022a.

818 Brodzik, S.: GOES IMPACTS, Dataset available online from the NASA Global
819   Hydrometeorology Resource Center DAAC, Huntsville, Alabama, U.S.A.,
820   https://doi.org/10.5067/IMPACTS/GOES/DATA101, 2022b.

821 Brown, P. R. A. and Francis, P. N.: Improved Measurements of the Ice Water Content in Cirrus
822   Using a Total-Water Probe, J. Atmos. Oceanic Technol., 12, 410–414,
823   https://doi.org/10.1175/1520-0426(1995)012<0410:IMOTIW>2.0.CO;2, 1995.

824 Chase, R. J., Nesbitt, S. W., and McFarquhar, G. M.: A Dual-Frequency Radar Retrieval of Two
825   Parameters of the Snowfall Particle Size Distribution Using a Neural Network, J. Appl.
826   Meteorol. Clim., 60, 341–359, https://doi.org/10.1175/JAMC-D-20-0177.1, 2021.

827 Cholette, M., Milbrandt, J. A., Morrison, H., Paquin-Ricard, D., and Jacques, D.: Combining
828   Triple-Moment Ice with Prognostic Liquid Fraction in the P3 Microphysics Scheme:
829   Impacts on a Simulated Squall Line, J. Adv. Model Earth Sy., 15, e2022MS003328,
830   https://doi.org/10.1029/2022MS003328, 2023.

831 Colle, B. A., Garvert, M. F., Wolfe, J. B., Mass, C. F., and Woods, C. P.: The 13–14 December
832   2001 IMPROVE-2 Event. Part III: Simulated Microphysical Budgets and Sensitivity
833   Studies, J. Atmos. Sci., 62, 3535–3558, https://doi.org/10.1175/JAS3552.1, 2005.

834 Connolly, P. J., Emersic, C., and Field, P. R.: A Laboratory Investigation into the Aggregation
835   Efficiency of Small Ice Crystals, Atmos. Chem. Phys., 12, 2055–2076,
836   https://doi.org/10.5194/acp-12-2055-2012, 2012.

837 DeLaFrance, A., McMurdie, L. A., Rowe, A. K., and Conrick, R.: Effects of Riming on Ice-
838   Phase Precipitation Growth and Transport Over an Orographic Barrier, J. Adv. Model
839   Earth Sy., 16, e2023MS003778, https://doi.org/10.1029/2023MS003778, 2024.

840 Field, P. R., Hogan, R. J., Brown, P. R. A., Illingworth, A. J., Choularton, T. W., and Cotton, R.
841   J.: Parametrization of Ice-Particle Size Distributions for Mid-Latitude Stratiform Cloud,
842   Q. J. Roy. Meteor. Soc., 131, 1997–2017, https://doi.org/10.1256/qj.04.134, 2005.

843 Field, P. R., Heymsfield, A. J., and Bansemer, A.: Snow Size Distribution Parameterization for
844   Midlatitude and Tropical Ice Clouds, J. Atmos. Sci., 64, 4346–4365,
845   https://doi.org/10.1175/2007JAS2344.1, 2007.

846 Grecu, M., Olson, W. S., Munchak, S. J., Ringerud, S., Liao, L., Haddad, Z., Kelley, B. L., and
847   McLaughlin, S. F.: The GPM Combined Algorithm, J. Atmos. Ocean Tech., 33, 2225–
848   2245, https://doi.org/10.1175/JTECH-D-16-0019.1, 2016.

849 Hersbach, H., Bell, B., Berrisford, P., Hirahara, S., Horányi, A., Muñoz-Sabater, J., Nicolas, J.,
850   Peubey, C., Radu, R., Schepers, D., Simmons, A., Soci, C., Abdalla, S., Abellan, X.,
851   Balsamo, G., Bechtold, P., Biavati, G., Bidlot, J., Bonavita, M., De Chiara, G., Dahlgren,
852   P., Dee, D., Diamantakis, M., Dragani, R., Flemming, J., Forbes, R., Fuentes, M., Geer,
853   A., Haimberger, L., Healy, S., Hogan, R. J., Hólm, E., Janisková, M., Keeley, S.,
854   Laloyaux, P., Lopez, P., Lupu, C., Radnoti, G., De Rosnay, P., Rozum, I., Vamborg, F.,
855   Villaume, S., and Thépaut, J.: The ERA5 Global Reanalysis, Q. J. Roy. Meteor. Soc.,
856   146, 1999–2049, https://doi.org/10.1002/qj.3803, 2020.

857 Heymsfield, A. J.: A Comparative Study of the Rates of Development of Potential Graupel and
858   Hail Embryos in High Plains Storms, J. Atmos. Sci., 39, 2867–2897,
859   https://doi.org/10.1175/1520-0469(1982)039<2867:ACSOTR>2.0.CO;2, 1982.

860 Heymsfield, A. J., Bansemer, A., Schmitt, C., Twohy, C., and Poellot, M. R.: Effective Ice
861   Particle Densities Derived from Aircraft Data, J. Atmos. Sci., 61, 982–1003,
862   https://doi.org/10.1175/1520-0469(2004)061<0982:EIPDDF>2.0.CO;2, 2004.

Heymsfield, A. Bansemer, A., Heymsfield, G., Noone, D., Grecu, M., and Toohey, D.: Relationship of Multiwavelength Radar Measurements to Ice Microphysics from the IMPACTS Field Program, J. Appl. Meteorol. Clim., 62, 289–315, https://doi.org/10.1175/JAMC-D-22-0057.1, 2023.

Holton, J. R. and Hakim, G. J.: An Introduction to Dynamic Meteorology, 5th edition., Elsevier : Academic Press, Amsterdam, 532 pp., ISBN 0123848679, 2012.

Iguchi, T., Seto, S., Meneghini, R., Yoshida, N., Awaka, J., Le, M., Chandrasekhar, V., Brodzik, S., and Kubota, T.: GPM/DPR Level-2 Algorithm Theoretical Basis Document, https://www.eorc.jaxa.jp/GPM/doc/algorithm/ATBD_DPR_201811_with_Appendix3b.pdf, last access: May 2024, 2018.

Jensen, A. A. and Harrington, J. Y.: Modeling Ice Crystal Aspect Ratio Evolution during Riming: A Single-Particle Growth Model, J. Atmos. Sci., 72, 2569–2590, https://doi.org/10.1175/JAS-D-14-0297.1, 2015.

Jensen, A. A., Harrington, J. Y., Morrison, H., and Milbrandt, J. A.: Predicting Ice Shape Evolution in a Bulk Microphysics Model, J. Atmos. Sci., 74, 2081–2104, https://doi.org/10.1175/JAS-D-16-0350.1, 2017.

Kalesse, H., Szyrmer, W., Kneifel, S., Kollias, P., and Luke, E.: Fingerprints of a Riming Event on Cloud Radar Doppler Spectra: Observations and Modeling, Atmos. Chem. Phys., 16, 2997–3012, https://doi.org/10.5194/acp-16-2997-2016, 2016.

Kneifel, S., Kollias, P., Battaglia, A., Leinonen, J., Maahn, M., Kalesse, H., and Tridon, F.: First Observations of Triple-Frequency Radar Doppler Spectra in Snowfall: Interpretation and Applications, Geophys. Res. Lett., 43, 2225–2233, https://doi.org/10.1002/2015GL067618, 2016.

Lawson, R. P., Stewart, R. E., Strapp, J. W., and Isaac, G. A.: Aircraft Observations of the Origin and Growth of Very Large Snowflakes, Geophys. Res. Lett., 20, 53–56, https://doi.org/10.1029/92GL02917, 1993.

Lawson, R. P., O'Connor, D., Zmarzly, P., Weaver, K., Baker, B., Mo, Q., and Jonsson, H.: The 2D-S (Stereo) Probe: Design and Preliminary Tests of a New Airborne, High-Speed, High-Resolution Particle Imaging Probe, J. Atmos. and Oceanic Tech., 23, 1462–1477, https://doi.org/10.1175/JTECH1927.1, 2006.

Lawson, R. P., Gurganus, C., Woods, S., and Bruintjes, R.: Aircraft Observations of Cumulus Microphysics Ranging from the Tropics to Midlatitudes: Implications for a "New" Secondary Ice Process, J. Atmos. Sci., 74, 2899–2920, https://doi.org/10.1175/JAS-D-17-0033.1, 2017.

Leinonen, J.: High-level Interface to T-matrix Scattering Calculations: Architecture, Capabilities and Limitations, Opt. Express, 22, 1655, https://doi.org/10.1364/OE.22.001655, 2014.

Leinonen, J. and Szyrmer, W.: Radar Signatures of Snowflake Riming: A Modeling Study, Earth Space Sci., 2, 346–358, https://doi.org/10.1002/2015EA000102, 2015.

Leinonen, J., Lebsock, M. D., Tanelli, S., Sy, O. O., Dolan, B., Chase, R. J., Finlon, J. A., Von Lerber, A., and Moisseev, D.: Retrieval of Snowflake Microphysical Properties from Multifrequency Radar Observations, Atmos. Meas. Tech., 11, 5471–5488, https://doi.org/10.5194/amt-11-5471-2018, 2018.

Li, L., Heymsfield, G., Carswell, J., Schaubert, D. H., McLinden, M. L., Creticos, J., Perrine, M., Coon, M., Cervantes, J. I., Vega, M., Guimond, S., Tian, L., and Emory, A.: The NASA High-Altitude Imaging Wind and Rain Airborne Profiler, IEEE T. Geosci. Remote, 54, 298–310, https://doi.org/10.1109/TGRS.2015.2456501, 2016.

Lin, Y. and Colle, B. A.: A New Bulk Microphysical Scheme That Includes Riming Intensity and Temperature-Dependent Ice Characteristics, Mon. Weather Rev., 139, 1013–1035, https://doi.org/10.1175/2010MWR3293.1, 2011.

Liu, G.: Approximation of Single Scattering Properties of Ice and Snow Particles for High Microwave Frequencies, J. Atmos. Sci., 61, 2441–2456, https://doi.org/10.1175/1520-0469(2004)061<2441:AOSSPO>2.0.CO;2, 2004.

Liu, G.: A Database of Microwave Single-Scattering Properties for Nonspherical Ice Particles, Bull. Amer. Meteor. Soc., 89, 1563–1570, https://doi.org/10.1175/2008BAMS2486.1, 2008.

Magono, C. and Lee, C. W.: Meteorological Classification of Natural Snow Crystals, J. Fac. Sci., Hokkaido University. Series 7, Geophysics, 2, 321–335, http://hdl.handle.net/2115/8672, 1966.

Mason, S. L., Chiu, C. J., Hogan, R. J., Moisseev, D., and Kneifel, S.: Retrievals of Riming and Snow Density from Vertically Pointing Doppler Radars, J. Geophys. Res.-Atmos., 123, https://doi.org/10.1029/2018JD028603, 2018.

Mason, S. L., Hogan, R. J., Westbrook, C. D., Kneifel, S., Moisseev, D., and Von Terzi, L.: The Importance of Particle Size Distribution and Internal Structure for Triple-Frequency Radar Retrievals of the Morphology of Snow, Atmos. Meas. Tech., 12, 4993–5018, https://doi.org/10.5194/amt-12-4993-2019, 2019.

Matrosov, S. Y.: Modeling Backscatter Properties of Snowfall at Millimeter Wavelengths, J. Atmos. Sci., 64, 1727–1736, https://doi.org/10.1175/JAS3904.1, 2007.

McLinden, M., Li, L., and Heymsfield, G. M.: High Altitude Imaging Wind and Rain Airborne Profiler (HIWRAP) IMPACTS, Dataset available online from the NASA Global Hydrometeorology Resource Center DAAC, Huntsville, Alabama, U.S.A., https://doi.org/10.5067/IMPACTS/HIWRAP/DATA101, 2022a.

McLinden, M., Li, L., and Heymsfield, G. M.: Cloud Radar System (CRS) IMPACTS, Dataset available online from the NASA Global Hydrometeorology Resource Center DAAC, Huntsville, Alabama, U.S.A., https://doi.org/10.5067/IMPACTS/CRS/DATA101, 2022b.

McMurdie, L. A., Heymsfield, G., Yorks, J. E., and Braun, S. A.: Investigation of Microphysics and Precipitation for Atlantic Coast-Threatening Snowstorms (IMPACTS) Collection. Dataset available online from the NASA Global Hydrometeorology Resource Center DAAC, Huntsville, Alabama, U.S.A., https://doi.org/10.5067/IMPACTS/DATA101, 2019.

McMurdie, L. A., Heymsfield, G. M., Yorks, J. E., Braun, S. A., Skofronick-Jackson, G., Rauber, R. M., Yuter, S., Colle, B., McFarquhar, G. M., Poellot, M., Novak, D. R., Lang, T. J., Kroodsma, R., McLinden, M., Oue, M., Kollias, P., Kumjian, M. R., Greybush, S. J., Heymsfield, A. J., Finlon, J. A., McDonald, V. L., and Nicholls, S.: Chasing Snowstorms: The Investigation of Microphysics and Precipitation for Atlantic Coast-Threatening Snowstorms (IMPACTS) Campaign, B. Am. Meteorol. Soc., 103, E1243–E1269, https://doi.org/10.1175/BAMS-D-20-0246.1, 2022.

Mishchenko, M. I., Travis, L. D., and Mackowski, D. W.: T-matrix Computations of Light Scattering by Nonspherical Particles: A Review, J. Quant. Spectrosc. Ra., 55, 535–575, https://doi.org/10.1016/0022-4073(96)00002-7, 1996.

Mishchenko, M. I. and Travis, L. D.: Capabilities and Limitations of a Current FORTRAN Implementation of the T-matrix Method for Randomly Oriented, Rotationally Symmetric

954   Scatterers, J. Quant. Spectrosc. Ra., 60, 309–324, https://doi.org/10.1016/S0022-
955   4073(98)00008-9, 1998.
956   Moisseev, D., Von Lerber, A., and Tiira, J.: Quantifying the Effect of Riming on Snowfall Using
957   Ground-Based Observations, J. Geophys. Res.-Atmos., 122, 4019–4037,
958   https://doi.org/10.1002/2016JD026272, 2017.
959   Morrison, H. and Milbrandt, J.: Comparison of Two-Moment Bulk Microphysics Schemes in
960   Idealized Supercell Thunderstorm Simulations, Mon. Wea. Rev., 139, 1103–1130,
961   https://doi.org/10.1175/2010MWR3433.1, 2011.
962   Morrison, H. and Milbrandt, J. A.: Parameterization of Cloud Microphysics Based on the
963   Prediction of Bulk Ice Particle Properties. Part I: Scheme Description and Idealized Tests,
964   J. Atmos. Sci., 72, 287–311, https://doi.org/10.1175/JAS-D-14-0065.1, 2015.
965   Morrison, H., Curry, J. A., and Khvorostyanov, V. I.: A New Double-Moment Microphysics
966   Parameterization for Application in Cloud and Climate Models. Part I: Description, J.
967   Atmos. Sci., 62, 1665–1677, https://doi.org/10.1175/JAS3446.1, 2005.
968   Morrison, H., Van Lier-Walqui, M., Fridlind, A. M., Grabowski, W. W., Harrington, J. Y.,
969   Hoose, C., Korolev, A., Kumjian, M. R., Milbrandt, J. A., Pawlowska, H., Posselt, D. J.,
970   Prat, O. P., Reimel, K. J., Shima, S., Van Diedenhoven, B., and Xue, L.: Confronting the
971   Challenge of Modeling Cloud and Precipitation Microphysics, J. Adv. Model Earth Sy.,
972   12, e2019MS001689, https://doi.org/10.1029/2019MS001689, 2020.
973   Novak, D. R., Bosart, L. F., Keyser, D., and Waldstreicher, J. S.: An Observational Study of
974   Cold Season–Banded Precipitation in Northeast U.S. Cyclones, Weather Forecast., 19,
975   993–1010, https://doi.org/10.1175/815.1, 2004.
976   Oue, M., Kollias, P., Ryzhkov, A., and Luke, E. P.: Toward Exploring the Synergy Between
977   Cloud Radar Polarimetry and Doppler Spectral Analysis in Deep Cold Precipitating
978   Systems in the Arctic, J. Geophys. Res.-Atmos., 123, 2797–2815,
979   https://doi.org/10.1002/2017JD027717, 2018.
980   Pruppacher, H. R. and Klett, J. D.: Microphysics of Clouds and Precipitation, 2nd rev. and enl.
981   ed., Kluwer Academic Publishers, Dordrecht ; Boston, 954 pp.,
982   https://doi.org/10.1007/978-0-306-48100-0, 1997.
983   Purcell, E. M. and Pennypacker, C. R.: Scattering and Absorption of Light by Nonspherical
984   Dielectric Grains, Astrophys. J., 186, 705, https://doi.org/10.1086/152538, 1973.
985   Shima, S., Kusano, K., Kawano, A., Sugiyama, T., and Kawahara, S.: The Super-Droplet
986   Method for the Numerical Simulation of Clouds and Precipitation: A Particle-Based and
987   Probabilistic Microphysics Model Coupled with a Non-Hydrostatic Model, Q. J. Roy.
988   Meteor. Soc., 135, 1307–1320, https://doi.org/10.1002/qj.441, 2009.
989   Skofronick-Jackson, G., Petersen, W. A., Berg, W., Kidd, C., Stocker, E. F., Kirschbaum, D. B.,
990   Kakar, R., Braun, S. A., Huffman, G. J., Iguchi, T., Kirstetter, P. E., Kummerow, C.,
991   Meneghini, R., Oki, R., Olson, W. S., Takayabu, Y. N., Furukawa, K., and Wilheit, T.:
992   The Global Precipitation Measurement (GPM) Mission for Science and Society, B. Am.
993   Meteorol. Soc., 98, 1679–1695, https://doi.org/10.1175/BAMS-D-15-00306.1, 2017.
994   Speirs, P., Gabella, M., and Berne, A.: A Comparison Between the GPM Dual-Frequency
995   Precipitation Radar and Ground-Based Radar Precipitation Rate Estimates in the Swiss
996   Alps and Plateau, J. Hydrometeorol., 18, 1247–1269, https://doi.org/10.1175/JHM-D-16-
997   0085.1, 2017.
998   Thornhill, K. L.: Turbulent Air Motion Measurement System (TAMMS) IMPACTS, Dataset
999   available online from the NASA Global Hydrometeorology Resource Center DAAC,

Huntsville, Alabama, U.S.A., https://doi.org/10.5067/IMPACTS/TAMMS/DATA101, 2022.

Thornhill, K. L., Anderson, B. E., Barrick, J. D. W., Bagwell, D. R., Friesen, R., and Lenschow, D. H.: Air Motion Intercomparison Flights During Transport and Chemical Evolution in the Pacific (TRACE-P)/ACE-ASIA, J. Geophys. Res.-Atmos., 108, 2002JD003108, https://doi.org/10.1029/2002JD003108, 2003.

Tridon, F., Battaglia, A., Chase, R. J., Turk, F. J., Leinonen, J., Kneifel, S., Mroz, K., Finlon, J., Bansemer, A., Tanelli, S., Heymsfield, A. J., and Nesbitt, S. W.: The Microphysics of Stratiform Precipitation During OLYMPEX: Compatibility Between Triple-Frequency Radar and Airborne In Situ Observations, J. Geophys. Res.-Atmos., 124, 8764–8792, https://doi.org/10.1029/2018JD029858, 2019.

Uccellini, L. W. and Kocin, P. J.: The Interaction of Jet Streak Circulations during Heavy Snow Events along the East Coast of the United States, Weather Forecast., 2, 289–308, https://doi.org/10.1175/1520-0434(1987)002<0289:TIOJSC>2.0.CO;2, 1987.

Van Weverberg, K., Vogelmann, A. M., Morrison, H., and Milbrandt, J. A.: Sensitivity of Idealized Squall-Line Simulations to the Level of Complexity Used in Two-Moment Bulk Microphysics Schemes, Mon. Wea. Rev., 140, 1883–1907, https://doi.org/10.1175/MWR-D-11-00120.1, 2012.

Waldstreicher, J. and Brodzik, S.: NOAA Sounding IMPACTS, Dataset available online from the NASA Global Hydrometeorology Resource Center DAAC, Huntsville, Alabama, U.S.A., https://doi.org/10.5067/IMPACTS/SOUNDING/DATA201, 2022.

Williams, C. R.: How Much Attenuation Extinguishes mm-Wave Vertically Pointing Radar Return Signals?, Remote Sens., 14, 1305, https://doi.org/10.3390/rs14061305, 2022.

Zaremba, T. J., Rauber, R. M., Heimes, K., Yorks, J. E., Finlon, J. A., Nicholls, S. D., Selmer, P., McMurdie, L. A., and McFarquhar, G. M.: Cloud-Top Phase Characterization of Extratropical Cyclones over the Northeast and Midwest United States: Results from IMPACTS. Journal Atmos. Sci., 81, 341-361. https://doi.org/10.1175/JAS-D-23-0123.1, 2024.

Zhang, J., Howard, K., Langston, C., Vasiloff, S., Kaney, B., Arthur, A., Van Cooten, S., Kelleher, K., Kitzmiller, D., Ding, F., Seo, D-J., Wells, E., and Dempsey C.: National Mosaic and Multi-Sensor QPE (NMQ) System: Description, Results, and Future Plans, Bull. Amer. Meteor. Soc., 92, 1321- 1338, https://doi.org/10.1175/2011BAMS-D-11-00047.1, 2011.